Chemical Science

ROYAL SOCIETY OF CHEMISTRY

EDGE ARTICLE

View Article Online
View Journal | View Issue

Cite this: *Chem. Sci.*, 2023, **14**, 6348

All publication charges for this article have been paid for by the Royal Society of Chemistry

Received 4th April 2023
Accepted 17th May 2023

DOI: 10.1039/d3sc01730c

rsc.li/chemical-science

Precise peripheral design enables propeller-like squaraine dye with highly sensitive and wide-range piezochromism†

Weihan Guo,[a] Mingda Wang,[a] Leilei Si,[a] Yigang Wang,[a] Guomin Xia *[a] and Hongming Wang [ab]

Piezochromic fluorescent (PCF) materials that feature high sensitivity and wide-range switching are attractive in intelligent optoelectronic applications but their fabrication remains a significant challenge. Here we present a propeller-like squaraine dye SQ-NMe_2 decorated with four peripheral dimethylamines acting as electron donors and spatial obstacles. This precise peripheral design is expected to loosen the molecular packing pattern and facilitate more substantial intramolecular charge transfer (ICT) switching caused by conformational planarization under mechanical stimuli. As such, the pristine SQ-NMe_2 microcrystal exhibits significant fluorescence changes from yellow (λ_{em} = 554 nm) to orange (λ_{em} = 590 nm) upon slight mechanical grinding and further to deep red (λ_{em} = 648 nm) upon heavy mechanical grinding. Single-crystal X-ray diffraction structural analysis of two SQ-NMe_2 polymorphs provides direct evidence to illustrate the design concept of such a piezochromic molecule. The piezochromic behavior of SQ-NMe_2 microcrystals is sensitive, high-contrast, and easily reversible, enabling cryptographic applications.

Introduction

Recently piezochromic fluorescent (PCF) materials with fluorescence properties changed under mechanical stimuli (pressure, grinding, stretching, or shearing) have garnered much interest from researchers in intelligent optoelectronic fields.[1–5] Since the seminal work of 1957,[6] the field of PCF materials has significantly flourished by exploiting purely organic luminophores.[7–12] During this process, molecular packing rearrangements,[13–15] molecular conformational changes,[16,17] and bond breaking[18,19] have been well assigned to cause their piezochromic behavior.[20] Nevertheless, due to small-shifted luminescence spectra upon mechanical stimuli, most PCF materials exhibit inconspicuous color switching.[21,22] This is mainly attributed to the fact that a universal design principle of PCF materials is less well established and the pressure-induced severe π–π interaction in π-conjugated PCF molecules thus quenches their luminescence rather than luminescence spectra shifting.[23,24]

The highly twisted π-conjugated stereogeometry intrinsically suppresses the π–π interaction and facilitates molecular conformational planarization under mechanical stimuli, thus being a privileged candidate in the fabrication of PCF materials.[25,26] In this regard, the natural propeller shape of tetraphenylethylene (TPE) and triphenylamine (TPA) makes them highly suitable for the test of the molecular conformational effect on piezochromism,[27] despite requiring very high pressure on the order of GPa.[28] Subsequent research further found that the piezochromic behaviors of TPE/TPA derivatives can become more effortless and highly tunable when stimuli-sensitive intramolecular charge transfer (ICT) features are brought on the TPE/TPA skeleton.[29–31] These findings tentatively establish a specific stereogeometry, that of highly distorted molecular conformations with ICT features, which may serve as a concise but more precise molecular design guideline for high-performance PCF materials.[32,33]

Squaraine dyes (SQs), with strong absorption and emission in a wide-range spectrum region, are classical organic dyes applied in advanced optoelectronic fields.[34–38] The SQ molecule bearing two diphenylamine moieties is documented as an aggregation-induced emission (AIE)-active luminogen,[39] adopting a centrosymmetric molecular conformation and propeller-like shape with intrinsic ICT features. With this in mind, here we present propeller-like SQ-NMe_2 with four peripheral dimethylamines that act as both electron donors and spatial obstacles (Fig. 1a). This precise peripheral design is expected to enhance its ICT effect further and cause multiple "soft

[a]*Institute for Advanced Study, Nanchang University, Nanchang 330031, China. E-mail: guominxia@ncu.edu.cn*

[b]*College of Chemistry and Chemical Engineering, Nanchang University, Nanchang 330031, China*

† Electronic supplementary information (ESI) available. CCDC SQ-H: 2239032, SQ-OMe: 2239031, SQ-NMe_2 Y-form: 2248407, and SQ-NMe_2 O-form: 2248408. For ESI and crystallographic data in CIF or other electronic format see DOI: https://doi.org/10.1039/d3sc01730c

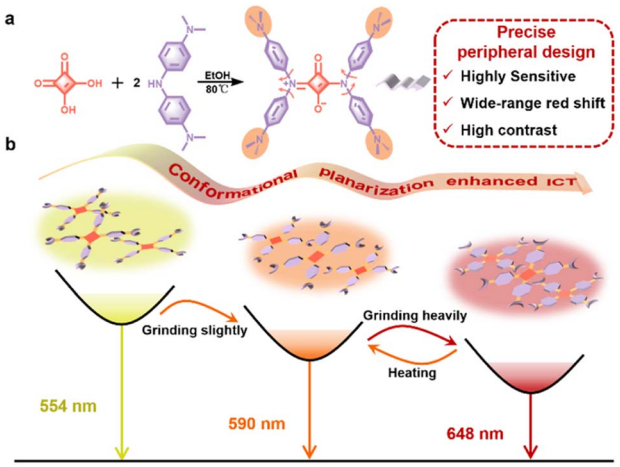

Fig. 1 (a) Synthesis route, molecular structure, and main advantages of PCF-active SQ-NMe_2. (b) Proposed mechanism of molecular conformation changes of SQ-NMe_2 microcrystals during the pressure-heating process.

interactions" (such as C–H···π and C–H···N/O interactions) to loosen the molecular packing pattern,[40–42] which both are crucial to the sensitivity and switching range under mechanical stimuli. Eventually, we demonstrated the highly sensitive and wide-range piezochromic switching of SQ-NMe_2 microcrystals under mechanical grinding (Fig. 1b and Table S1†), and theoretical calculations and single crystal X-ray diffraction analyses directly proved the mechanism. Cryptographic applications with good recovery and high contrast have also been demonstrated based on SQ-NMe_2 microcrystals.

Results and discussion

The synthesis route and structural characterization of SQ-NMe_2 are detailed in the ESI.† In common organic solvents, the UV-vis absorption spectra of SQ-NMe_2 were recorded with a maximum absorption peak (λ_{ab}) centered at 460 nm (Fig. S1†), and no fluorescence emission was observed. In *N*,*N*-dimethylformamide (DMF)/water mixtures, SQ-NMe_2 remains non-emissive with the increase of water fractions (f_w) from 0% to 40%; after that, the amorphism emissions with the maximum peak (λ_{em}) around 583 nm increased rapidly together with tiny nanoparticles appeared, suggesting a typical AIE characteristic (Fig. S2†).[43,44]

SQ-NMe_2 has a high crystallization tendency, probably ascribed to its multiple intermolecular interactions (such as C–H···π and C–H···N/O interactions).[45] The SQ-NMe_2 microcrystals can be facilely obtained by recrystallization in DMF and methanol (for details see the ESI†). As shown in Fig. 2a and b, these microcrystals showed a strong yellow emission with λ_{em} at 554 nm and a fluorescence quantum yield (Φ_{PL}) of 36.9%. When scraping these pristine SQ-NMe_2 microcrystals with a spatula, apparent changes in the UV-vis and emission colors can be easily observed. As such, we then examined the complete PCF behaviors of these microcrystals. Upon being slightly ground with a pestle for only 1 min, the emission color of these

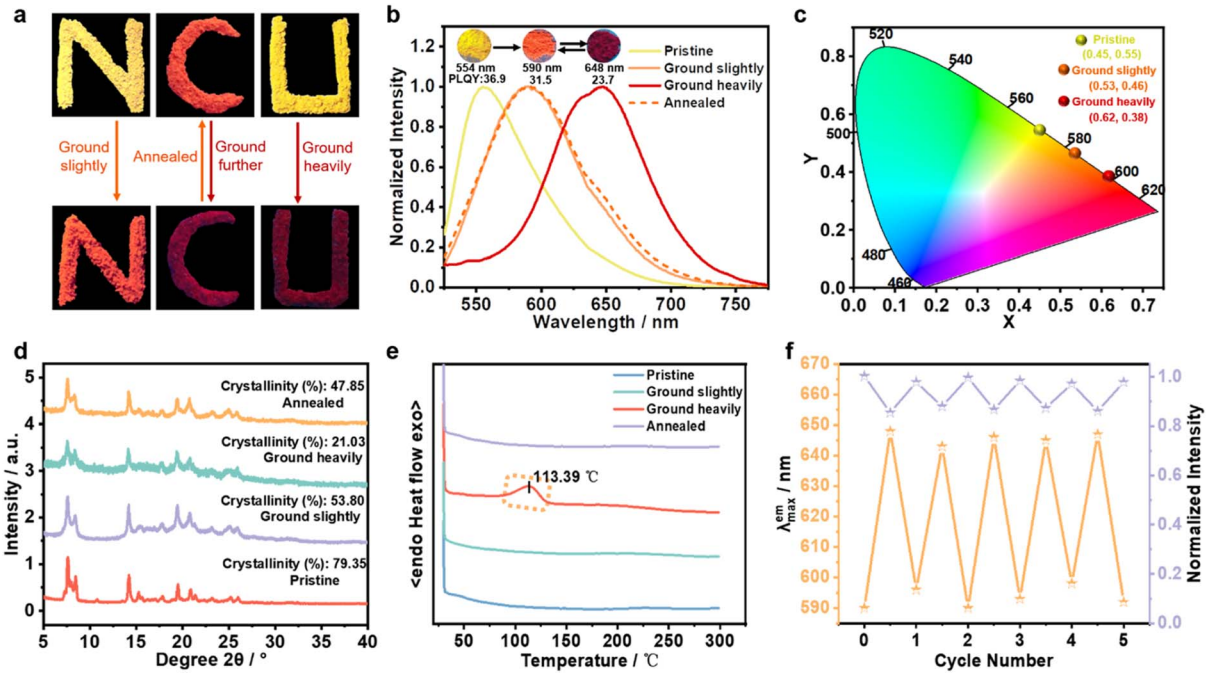

Fig. 2 (a) Fluorescence photographs of pristine and treated SQ-NMe_2 microcrystals under UV light illumination (365 nm). (b) Normalized PL spectra of pristine SQ-NMe_2 microcrystals during grinding (solid line) and subsequent annealing (dotted line) processes (inset: corresponding PL photographs). (c) CIE coordinate diagram of SQ-NMe_2 microcrystals during the gradual grinding process. (d) PXRD patterns and (e) DSC curves of pristine and treated SQ-NMe_2 microcrystals. The scan rate is 20 °C min^{-1} under N_2. (f) Cyclic switch of the wavelength and intensity during the grinding–heating process.

microcrystals fully changed from yellow to orange with λ_{em} redshifted to 590 nm, and Φ_{PL} decreased a bit to 31.5%. Upon further grinding heavily for 5 min, deep red emission with λ_{em} at 648 nm appeared, and Φ_{PL} further lowed to 23.7%. After more than twenty minutes of continuous grinding, no new red-shifted peaks were recorded. Furthermore, after heating at 140 °C for only 1 min, the deep red emission of these heavily ground SQ-NMe_2 microcrystals was back to orange emission. At the same time, continuous heating did not restore its yellow emission any further. We plotted Commission International de L'Éclairage (CIE) 1931 coordinates (Fig. 2c), showing a wide-range redshift of the piezochromic process. The redshift in the λ_{ab} of pristine SQ-NMe_2 microcrystals further corroborated the red-shifted emission from grinding (Fig. S3†). The lifetime decay profiles of SQ-NMe_2 microcrystals in the piezochromic process were tested by single photo-counting, showing approximately short lifetimes of 1.65 ns, 1.32 ns, and 1.26 ns for the yellow, orange, and deep red ones, respectively (Fig. S4†). All the photophysical data of SQ-NMe_2 microcrystals are summarized in Table S2.†

To essentially understand their microstructure, powder X-ray diffraction (PXRD) measurement was performed on SQ-NMe_2 microcrystals that were treated under different conditions. The results show that SQ-NMe_2 microcrystals transitioned from well-order crystalline to amorphous during the gradual grinding. As shown in Fig. 2d, the number and intensity of diffraction peaks decreased with gradual grinding of pristine SQ-NMe_2 microcrystals, which can be revealed by tapering crystallinity from 79.35% to 53.8% to 21.03%. Not surprisingly, the annealed SQ-NMe_2 powders restored to the crystalline phase with crystallinity increasing to 47.85%, similar to slightly ground SQ-NMe_2 microcrystals. The differential scanning calorimetry (DSC) curves revealed that the heavily ground SQ-NMe_2 powders display a cold-crystallization transition peak at 113.39 °C (Fig. 2e), which supports the heat treatment temperature of 140 °C in the above recoverability testing. Meanwhile, the DSC curve of the slightly ground SQ-NMe_2 microcrystals showed no peak, which matched well with the fact that continuous heating cannot restore its orange emission to yellow any further. In other words, this DSC curve showed that the ground powders were in the metastable amorphous phase and converted into a stable crystalline phase *via* external thermal recrystallizing. Moreover, the grinding–heating rewritable test demonstrated that the SQ-NMe_2 emission cyclic process between orange and deep red could be repeated at least five times, which provides its practical possibility (Fig. 2f and S5†).

Fortunately, high-quality needle-like crystals were found in preparing pristine SQ-NMe_2 microcrystals, which is suitable for single-crystal XRD analysis (termed as Y-form). The PXRD patterns of pristine SQ-NMe_2 microcrystals coincided with their simulated XRD patterns, suggesting the same molecular packing modes (Table S3, Fig. S6 and S8†). In Fig. 3a(i), the torsion angles between the four-membered ring and diphenylamine moieties in SQ-NMe_2 Y-form were determined to be approximately 29° and 65°. There is a type of weak Ar–H···O hydrogen bonding interaction of 2.860 Å between Ar–H and carbonyl at the four-membered ring, which restrains one of the dihedral angles to 65°. Two types of hydrogen bonding interaction that restrains the dihedral angles to 29° were observed, one was Ar–H···N of 3.004 Å and the other was Ar–H···π of 3.012 Å between adjacent SQ-NMe_2 molecules (Fig. 3a(ii)). There is no π–π overlap in SQ-NMe_2 Y-form, accounting for its efficient yellow emission.[46–48] More importantly, such two types of hydrogen bonding interactions belong to the so-called "soft interactions" and good response to the sensitive PCF behaviors of SQ-NMe_2 Y-form.

By slow evaporation in dichloromethane, another orange needle-like SQ-NMe_2 single-crystal was cultured, termed O-form (Table S3, Fig. S6 and S8†). Single-crystal XRD analysis revealed that the torsion angles between the four-membered ring and diphenylamine moieties in SQ-NMe_2 O-form ranged from 33° to 43° (Fig. 3b(i)), which were smaller compared to that of the Y-form. There is also no π–π overlap in SQ-NMe_2 O-form (Fig. 3b(ii)), and simultaneously the emission spectrum of SQ-NMe_2 O-form turned out to be very similar to that of slightly ground SQ-NMe_2 microcrystals (Fig. S9 and S10†), implying their quite similar molecular conformations. As such, it was concluded that the red-shifted emission of pristine SQ-NMe_2 microcrystals was possibly derived from the molecular conformational planarization-induced ICT enhancement after slight grinding. Multiple Ar–H···π and Ar–H···N hydrogen bonding interactions were observed with the distance ranging from 2.699 to 3.142 Å between adjacent molecules in SQ-NMe_2 O-form (Fig. 3b(ii)). These interactions, maintaining the dihedral angles of the four-membered ring and diphenylamine moieties, were richer and slightly more potent than the Y-form but still soft. These observations thus account for the deep red emission of orange SQ-NMe_2 microcrystals arising from further conformational planarization under heavy grinding. Detailed single-crystal analyses of these two SQ-NMe_2 polymorphs have been deciphered in the ESI (Fig. S11 and S12).†

In order to verify the significance of "soft interactions" in the piezochromic behaviors of SQ-NMe_2 microcrystals, we designed and synthesized SQ-H and SQ-OMe as the control group (for synthesis methods and characterization see the ESI†). Their corresponding single crystals were easily obtained and the single-crystal XRD analyses are further detailed in the ESI (Table S4, Fig. S13 and S15).† As shown in Fig. 3c and d, there are multiple moderate to strong Ar–H···O and Ar–H···π interactions locking the phenyl rotations of SQ-H and SQ-OMe and subsequent ICT switching. These differences in their stereogeometry, compared to SQ-NMe_2, enhance their intramolecular rigidity in crystals and will suppress their piezochromism. Not surprisingly, SQ-H and SQ-OMe microcrystals exhibited no PCF behavior, and their PXRD patterns didn't show obvious change upon grinding and heating (Fig. S16 and S17†). All those crystal structure analyses indicate that the "soft interactions" caused by the peripheral dimethylamines loosen the molecular packing pattern in such propeller-like squaraine dye, thus triggering highly sensitive and wide-range piezochromism of SQ-NMe_2 microcrystals. Like SQ-NMe_2, the photophysical and structural characterization of SQ-H and SQ-OMe was also conducted, which is detailed in the ESI (Fig. S18, S22 and Table S5).†

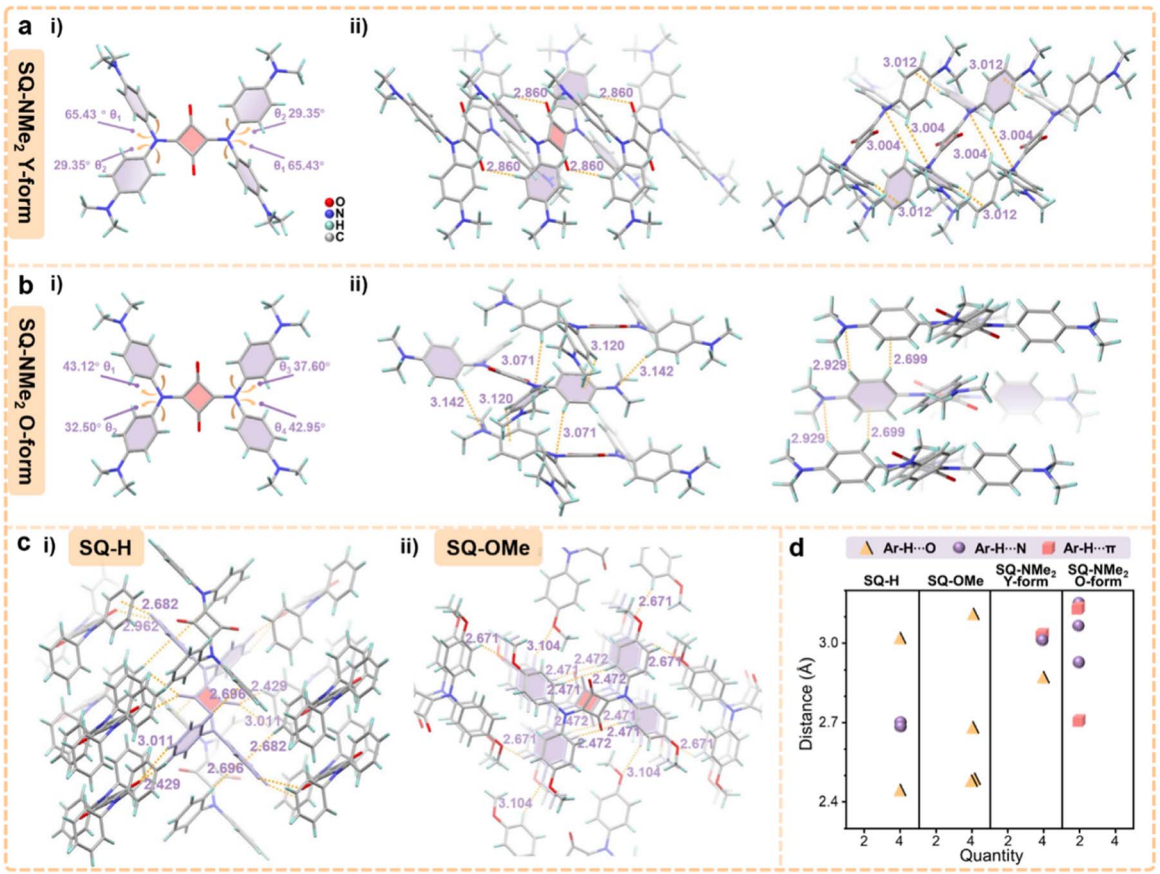

Fig. 3 (a) Structural analysis of SQ-NMe_2 in a Y-form crystal. (i) The torsion angles of SQ-NMe_2. (ii) The intermolecular interactions for locking the phenyl rotations between adjacent SQ-NMe_2. (b) Structural analysis of SQ-NMe_2 in an O-form crystal. (i) The torsion angles of SQ-NMe_2. (ii) The intermolecular interactions for locking the phenyl rotations between adjacent SQ-NMe_2. (The incorporated dichloromethane solvent is omitted.) (c) The multiple Ar–H···O and Ar–H···π hydrogen bonding interactions for locking the phenyl rotations in (i) SQ-H and (ii) SQ-OMe crystals. (d) Statistical chart of intermolecular interactions for locking the phenyl rotations in these four crystals.

To further understand the optical behaviors, the absorption of SQ-NMe_2 in the gas state was calculated at B3LYP/6-31G(d)[49,50] by Gaussian 09, which can be all attributed to the $S_0 \rightarrow S_1$ transition, corresponding to the highest occupied molecular orbital (HOMO) → lowest unoccupied molecular orbital (LUMO) transition. The λ_{ab} was calculated to be 439 nm, which matched well with the experimental result. Meanwhile, the calculated absorption of SQ-H and SQ-OMe was similar to that of SQ-NMe_2 (Table S6 and Fig. S23†).

To explain the primary cause of why SQ-NMe_2 shows distinct emissions at varying torsion angles, the emission spectra of four kinds of fixed conformation were recorded (for details see the ESI†).[51,52] As shown in Fig. 4, the π-conjugation of the diphenylamine donor and central ring acceptor on the HUMO was strengthened with the torsion angle decrease, resulting in overlapping frontier orbitals and their enhanced coplanarity. Meanwhile, it is demonstrated that the electron density spread over the whole molecule skeleton on the HUMO, while that on the LUMO was more distributed in the central four-membered ring, which meant an ICT state in the excited state. Consequently, decreasing the torsion angle in these four SQ-NMe_2 accompanies enhancing the ICT effect, facilitating the redshift of emission spectra. Moreover, this trend is highly consistent with the experimental results. Combined with the analyses of yellow and orange SQ-NMe_2 single crystals, these calculations further confirmed that the deep red emission arises from the conformational planarization of SQ-NMe_2 molecules upon heavy grinding. Notably, the peripheral dimethylamines in SQ-NMe_2 contribute much to this ICT process, consistent with the wide-range piezochromism. The difference between the experimental and the calculated emission may be because the intermolecular interactions did not take into account, which is essential in the crystal state.

Because of the high contrast emission color, the information constituted by orange SQ-NMe_2 O-form and the deep red ground powders has high resolution. Moreover, we surprisingly found that the emission color of SQ-OMe microcrystals was approximate to that of SQ-NMe_2 O-form (Fig. S24†). Therefore, meeting the need for modern applications, we printed a complicated quick response (QR) code with crystalline SQ-OMe and SQ-NMe_2 O-form, which can achieve multi-level information encryption. As shown in Fig. 5, first, the QR code emitted orange fluorescence under UV light; after scanning with a smartphone, a login window appeared. After grinding the

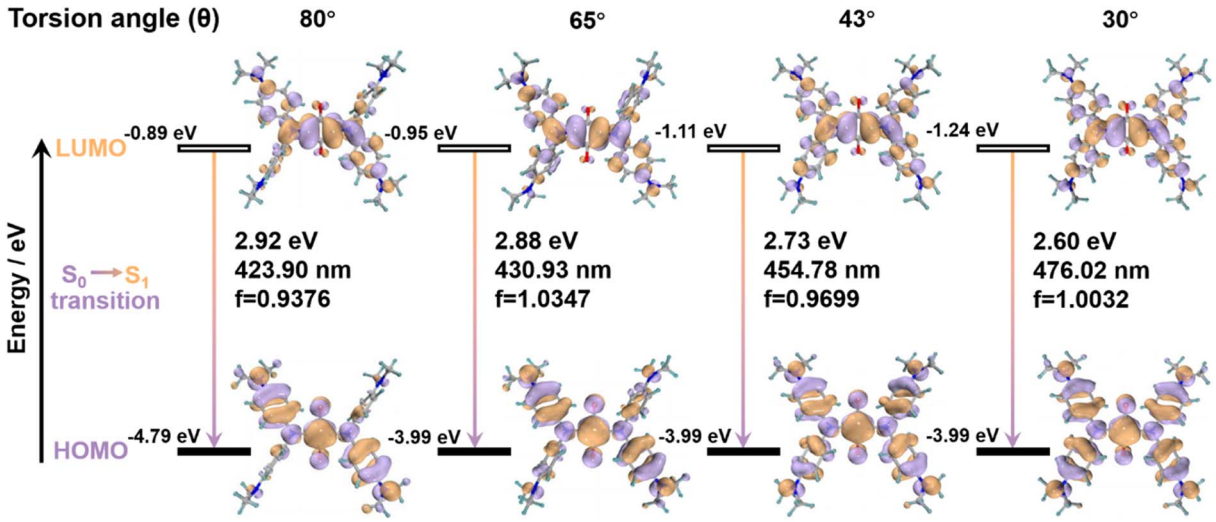

Fig. 4 Energy diagrams and the frontier orbital contribution of SQ-NMe_2 in a fixed conformation based on gradually decreased torsion angels (θ) between the central four-membered ring and diphenylamine rotors, together with their lowest-energy transitions estimated by theoretical calculations.

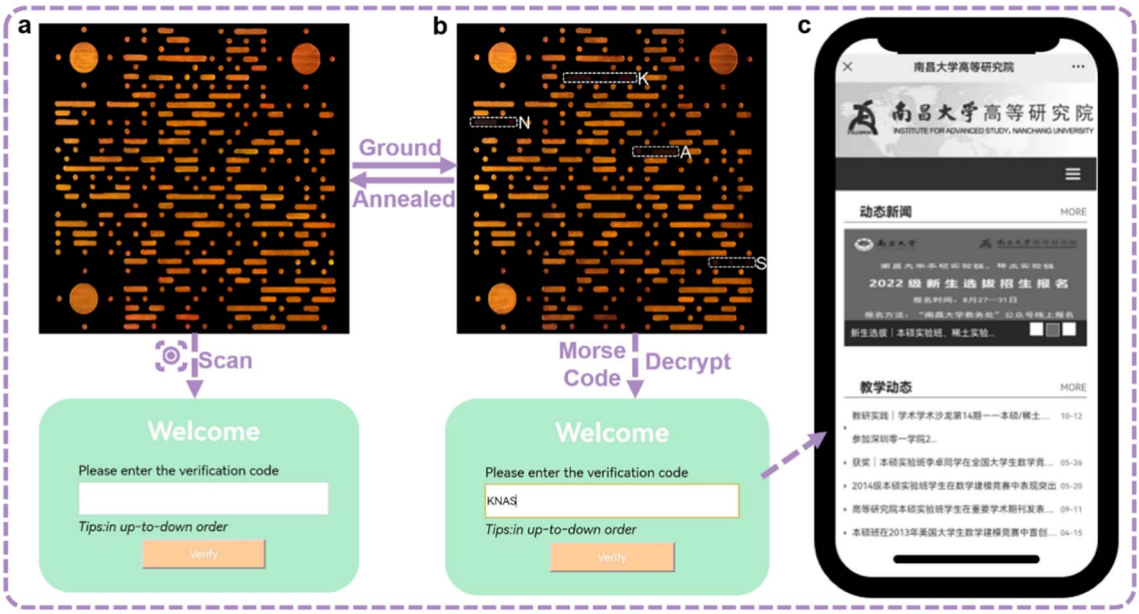

Fig. 5 A complicated QR code. (a) QR code with SQ-OMe and SQ-NMe_2 crystal phases is constructed, and a login window appears when scanning the code with a smartphone. (b) Grinding the QR code leads to the appearance of Morse signals, which are then translated into the letter sequence "KNAS". (c) The input of "KNAS" as the verification code allows access to the target website.

whole QR code, only part of the SQ-NMe_2 O-form became deep red, which demonstrated the Morse signals that can be translated into "KNAS" (Fig. S25†). Furthermore, the verification code "KNAS" was entered, and then the link automatically redirected to the target website (**https://ias.ncu.edu.cn/**). As the deep red emission of the obtained SQ-NMe_2 microcrystals can be annealed to orange and SQ-OMe has high thermal stability, the QR code can be recovered to the initial state after heating at 140 °C for only 1 min. The encryption and decryption of QR codes are just realized through the regulation of the crystal state under external mechanical stimuli, but not some complex chemical reactions or fumigation with an organic solvent. This provides a good reference for the future green and rewritable applications of PCF materials.

Conclusions

In summary, based on propeller-like squaraine dye, a precise peripheral design for highly sensitive and wide-range PCF materials was consciously proposed. Peripheral dimethylamines, acting as electron donors and spatial obstacles, were introduced into this highly twisted π-conjugated molecule.

Such a design can loosen the molecular packing pattern and easily facilitate more substantial ICT switching caused by conformational planarization under mechanical stimuli. As a result, SQ-NMe_2 microcrystals showed a highly sensitive spectral shift of their emission from yellow (λ_{em} = 554 nm) to deep red (λ_{em} = 648 nm) upon grinding. Multi-level cryptographic applications with good recovery and high contrast have also been achieved based on SQ-NMe_2 microcrystals. Our research provided new design guidance for developing excellent PCF materials with high sensitivity, wide-range switching, and good recovery.

Data availability

Additional experimental data supporting this article are included in the ESI.†

Author contributions

Weihan Guo conducted formal analysis, performed experimental measurements, and prepared the initial version of the manuscript. Mingda Wang performed the theoretical calculations. Leilei Si performed experimental measurements. Yigang Wang helped with the revision of the manuscript. Hongming Wang helped with the revision of the manuscript. Guomin Xia: formal analysis, supervision, and writing – review & editing.

Conflicts of interest

There are no conflicts to declare.

Acknowledgements

This work was supported by the National Natural Science Foundation of China (No 22063005), the Natural Science Foundation of Jiangxi Province (No. 20212ACBA203012 and No. 20224BAB214003), and the Interdisciplinary Innovation Fund of Natural Science, Nanchang University (No. 9167-27060003-ZD2101 and No. 9167-28220007-YB2113). The authors thank Xiaoyu Ye for the support of single-crystal XRD tests.

Notes and references

1 L. Wang, L. Liu, B. Xu and W. Tian, *Chem. Res. Chin. Univ.*, 2021, **37**, 100–109.
2 S. Mukherjee and P. Thilagar, *Angew. Chem., Int. Ed.*, 2019, **58**, 7922–7932.
3 L. Liu, X. Wang, N. Wang, T. Peng and S. Wang, *Angew. Chem., Int. Ed.*, 2017, **56**, 9160–9164.
4 Y. Sagara and T. Kato, *Nat. Chem.*, 2009, **1**, 605–610.
5 A. Li, Z. Li, M. Zhang, B. Wu, Y. Xing and L. Zhu, *Adv. Opt. Mater.*, 2022, **10**, 2102146.
6 A. Schönberg, A. E. K. Fateen and A. E. M. A. Sammour, *J. Am. Chem. Soc.*, 1957, **79**, 6020–6023.
7 C. Zhu, Q. Luo, Y. Shen, C. Lv, S. Zhao, X. Lv, F. Cao, K. Wang, Q. Song, C. Zhang and Y. Zhang, *Angew. Chem., Int. Ed.*, 2021, **60**, 8510–8514.
8 Y. Sagara, T. Mutai, I. Yoshikawa and K. Araki, *J. Am. Chem. Soc.*, 2007, **129**, 1520–1521.
9 D. Yan, J. Lu, J. Ma, S. Qin, M. Wei, D. G. Evans and X. Duan, *Angew. Chem., Int. Ed.*, 2011, **50**, 7037–7040.
10 C. Zhai, X. Yin, S. Niu, M. Yao, S. Hu, J. Dong, Y. Shang, Z. Wang, Q. Li, B. Sundqvist and B. Liu, *Nat. Commun.*, 2021, **12**, 4084.
11 J. Zou, Y. Fang, Y. Shen, Y. Xia, K. Wang, C. Zhang and Y. Zhang, *Angew. Chem., Int. Ed.*, 2022, **61**, e202207426.
12 X. Yin, C. Zhai, S. Hu, L. Yue, T. Xu, Z. Yao, Q. Li, R. Liu, M. Yao, B. Sundqvist and B. Liu, *Chem. Sci.*, 2023, **14**, 1479–1484.
13 J. Li, L. Gao, T. Lu, Z. Feng, D. Jiang, C. Du, K. Wang, P. Lu and B. Zou, *Adv. Opt. Mater.*, 2021, **9**, 2100813.
14 Z. Man, Z. Lv, Z. Xu, Q. Liao, J. Liu, Y. Liu, L. Fu, M. Liu, S. Bai and H. Fu, *Adv. Funct. Mater.*, 2020, **30**, 2000105.
15 W. Qiao, P. Yao, Y. Chen, Q. Xiao, L. Zhang and Z. Li, *Mater. Chem. Front.*, 2020, **4**, 2688.
16 T. Suzuki, H. Okada, T. Nakagawa, K. Komatsu, C. Fujimoto, H. Kagi and Y. Matsuo, *Chem. Sci.*, 2018, **9**, 475–482.
17 Y. Liu, Q. Zeng, B. Zou, Y. Liu, B. Xu and W. Tian, *Angew. Chem., Int. Ed.*, 2018, **57**, 15670–15674.
18 B. A. Versaw, M. E. McFadden, C. C. Husic and M. J. Robb, *Chem. Sci.*, 2020, **11**, 4525–4530.
19 Y. Wang, X. Tan, Y. M. Zhang, S. Zhu, I. Zhang, B. Yu, K. Wang, B. Yang, M. Li, B. Zou and S. X. Zhang, *J. Am. Chem. Soc.*, 2015, **137**, 931–939.
20 A. Li, S. Xu, C. Bi, Y. Geng, H. Cui and W. Xu, *Mater. Chem. Front.*, 2021, **5**, 2588–2606.
21 R. Li, S. Xiao, Y. Li, Q. Lin, R. Zhang, J. Zhao, C. Yang, K. Zou, D. Li and T. Yi, *Chem. Sci.*, 2014, **5**, 3922–3928.
22 Q. Di, J. Li, Z. Zhang, X. Yu, B. Tang, H. Zhang and H. Zhang, *Chem. Sci.*, 2021, **12**, 15423–15428.
23 J. V. Caspar, E. M. Kober, B. P. Sullivan and T. J. Meyer, *J. Am. Chem. Soc.*, 1982, **104**, 630.
24 J. S. Wilson, N. Chawdhury, M. R. A. Al-Mandhary, M. Younus, M. S. Khan, P. R. Raithby, A. Köhler and R. H. Friend, *J. Am. Chem. Soc.*, 2001, **123**, 9412.
25 Q. Qi, J. Zhang, B. Xu, B. Li, S. X.-A. Zhang and W. Tian, *J. Phys. Chem. C*, 2013, **117**, 24997–25003.
26 X. Wu, J. Guo, Y. Cao, J. Zhao, W. Jia, Y. Chen and D. Jia, *Chem. Sci.*, 2018, **9**, 5270–5277.
27 B. Xu, J. He, Y. Mu, Q. Zhu, S. Wu, Y. Wang, Y. Zhang, C. Jin, C. Lo, Z. Chi, A. Lien, S. Liu and J. Xu, *Chem. Sci.*, 2015, **6**, 3236–3241.
28 Q. Luo, C. Lv, H. Sheng, F. Cao, J. Sun, C. Zhang, M. Ouyang, B. Zou and Y. Zhang, *Adv. Opt. Mater.*, 2020, **8**, 1901836.
29 Q. Qi, J. Qian, X. Tan, J. Zhang, L. Wang, B. Xu, B. Zou and W. Tian, *Adv. Funct. Mater.*, 2015, **25**, 4005–4010.
30 Y. Zhang, J. Zhang, J. Shen, J. Sun, K. Wang, Z. Xie, H. Gao and B. Zou, *Adv. Opt. Mater.*, 2018, **6**, 1800956.
31 Y. Wang, I. Zhang, B. Yu, X. Fang, X. Su, Y.-M. Zhang, T. Zhang, B. Yang, M. Li and S. X.-A. Zhang, *J. Mater. Chem. C*, 2015, **3**, 12328–12334.
32 C. Lv, W. Liu, Q. Luo, H. Yi, H. Yu, Z. Yang, B. Zou and Y. Zhang, *Chem. Sci.*, 2020, **11**, 4007–4015.

33 J. Wang, B. Yue, X. Jia, R. Cao, X. Niu, H. Zhao, J. Li and L. Zhu, *Chem. Commun.*, 2022, **58**, 3517–3520.
34 W. Qiao, T. Ma, S. Wang, L. Li, M. Liu, H. Jiang, Y. Wu, J. Zhu and Z. a. Li, *Adv. Funct. Mater.*, 2021, **31**, 2105452.
35 W. Qiao and Z. a. Li, *Symmetry*, 2022, **14**, 966.
36 Q. Xiao, Y. Li, F. Wu, M. Han, M. Xie, Z. Li, L. Zhu and Z. a. Li, *J. Mater. Chem. C*, 2018, **6**, 10547–10556.
37 P. Yao, W. Qiao, Y. Wang, H. Peng, X. Xie and Z. a. Li, *Chem.–Eur. J.*, 2022, **28**, e202200725.
38 J. He, Y. J. Jo, X. Sun, W. Qiao, J. Ok, T. i. Kim and Z. a. Li, *Adv. Funct. Mater.*, 2021, **31**, 2008201.
39 Y. Ohsedo, M. Miyamoto, A. Tanaka and H. Watanabe, *Dyes Pigm.*, 2014, **101**, 261–269.
40 X. Wang, Q. Liu, H. Yan, Z. Liu, M. Yao, Q. Zhang, S. Gong and W. He, *Chem. Commun.*, 2015, **51**, 7497–7500.
41 Z. Lv, Z. Man, Z. Xu, L. Fu, S. Li, Y. Zhang and H. Fu, *Adv. Opt. Mater.*, 2021, **9**, 2100598.
42 R. H. Pawle, T. E. Haas, P. Müller and S. W. Thomas III, *Chem. Sci.*, 2014, **5**, 4184–4188.
43 S. Cho, T. S. Shim, J. H. Kim, D. H. Kim and S. H. Kim, *Adv. Mater.*, 2017, **29**, 1700256.
44 Z. Wu, S. Mo, L. Tan, B. Fang, Z. Su, Y. Zhang and M. Yin, *Small*, 2018, **14**, e1802524.
45 P. Chen, H. Zhang, L. Niu, Y. Zhang, Y. Chen, H. Fu and Q. Yang, *Adv. Funct. Mater.*, 2017, **27**, 1700332.
46 C. Feng, C. S. Lin, W. Fan, R. Q. Zhang and M. A. Van Hove, *J. Chem. Phys.*, 2009, **131**, 194702.
47 Z. Chen, A. Lohr, C. R. Saha-Moller and F. Wurthner, *Chem. Soc. Rev.*, 2009, **38**, 564–584.
48 R. Weinberger and L. C. Love, *Spectrochim. Acta, Part A*, 1984, **40**, 49–55.
49 C. T. Lee, W. T. Yang and R. G. Parr, *Phys. Rev. B: Condens. Matter Mater. Phys.*, 1988, **37**, 785.
50 A. D. Becke, *J. Chem. Phys.*, 1993, **98**, 5648–5652.
51 T. Lu and F. Chen, *J. Comput. Chem.*, 2012, **33**, 580–592.
52 W. Humphrey, A. Dalke and K. Schulten, *J. Mol. Graphics*, 1996, **14**, 33–38.